British Journal of Mathematics & Computer Science
7(5): 375-390, 2015, Article no.BJMCS.2015.132
ISSN: 2231-0851

SCIENCEDOMAIN *international*
www.sciencedomain.org

Large Eddy Simulation of Turbulent Channel Flow Using Smagorinsky Model and Effects of Smagorinsky Constants

M. Ashraf Uddin[1] and M. Saiful Islam Mallik[1,2*]

[1]Department of Mathematics, Shahjalal University of Science and Technology, Sylhet, Bangladesh.
[2]Department of Arts and Sciences, Ahsanullah University of Science and Technology, Dhaka, Bangladesh.

Article Information

DOI: 10.9734/BJMCS/2015/15962
Editor(s):
(1) Sergio Serrano, Department of Applied Mathematics, University of Zaragoza, Spain.
(2) Tian-Xiao He, Department of Mathematics and Computer Science, Illinois Wesleyan University, USA.
Reviewers:
(1) Luben Cabezas Gómez, Department of Mechanical Engineering, University of São Paulo, EESC-USP, Brazil.
(2) Anonymous, China.
(3) João Batista Campos Silva, Department of Mechanical Engineering, São Paulo State University – UNESP at Ilha Solteira, Brazil.
Complete Peer review History: http://www.sciencedomain.org/review-history.php?iid=936&id=6&aid=8300

Original Research Article

Received: 30 December 2014
Accepted: 10 February 2015
Published: 28 February 2015

Abstract

A large eddy simulation (LES) of a turbulent channel flow is performed by using the Smagorinsky subgrid scale model and the effects of Smagorinsky constants in LES are discussed. The computation is performed in the domain of $2\pi\delta\times 2\delta\times\pi\delta$ with $32\times 64\times 32$ grid points at a Reynolds number Re_τ = 590 based on the channel half width, δ and wall shear velocity, u_τ. The performance of the Smagorinsky model is tested in LES for three values of Smagorinsky constant, C_S = 0.065, 0.1 and 0.13, and for all three cases the computed essential turbulence statistics of the flow field are compared with Direct Numerical Simulation (DNS) data. Comparing the results with those from DNS data throughout the whole calculation domain we have found that turbulence statistics for C_S = 0.065 show reasonable agreement with the DNS data. Agreements as well as discrepancies are discussed. The behavior of the flow structures in the computed flow field has also been discussed.

Keywords: Large eddy simulation; turbulent channel flow; smagorinsky constant; staggered grid.

AMS-MSC 2010 No.: 76F65, 76D05

**Corresponding author: saiful1185@yahoo.com;*

1 Introduction

Turbulent channel flow has been widely considered as a benchmark for numerical simulations and validation of turbulence models. Its geometric simplicity is attractive for both experimental and theoretical investigations of complex turbulence interactions near a wall. As a result, a wide range of experimental and computational studies of turbulent channel flow have been carried out [1-7].

A simulation that resolves all flow scales is called direct numerical simulation (DNS), but the high computational cost of DNS makes it impractical for realistic engineering flows. An alternative approach to DNS is the large eddy simulation (LES) technique [5-14]. In LES, the computational cost is reduced by applying a low-pass filter to the turbulent flow, thereby eliminating many of the small scales below the filter width. In LES, the large-scale motion is exactly calculated, while the dynamical effects of the smaller scales resulting from the filtering operation are represented by subgrid scale (SGS) models [5,10]. In general, SGS models can capture these effects only partially.

Because of growing popularity of LES, recent research has been aimed at developing robust LES models and these models are derived based on some assumption about the nature of the subgrid turbulence. The most commonly used LES model is the well-known Smagorinsky model [15], which is based on the equilibrium assumption at the small scales. In this model the theoretical value of Smagorinsky constant, C_S is evaluated by some relations [15]. It should be noted that the value of this constant is, in practice, adjusted to improve the results. By trial it is believed that the optimum value of the Smagorinsky constant decreases with the increase of mean shear. But the exact cause for the dependence of C_S on mean shear is not completely understood. Horiuti [12] and Yakhot et al. [13] speculate that the anisotropy of the SGS motions is significant near a bounding surface. It is also believed that the Smagorinsky constant also varies with grid mesh aspect ratio as pointed out by Scotti et al. [16]. For instance, in channel flows, Deardorff [3] and Piomelli *et al.* [7] use C_S = 0.1; Bardina [14] finds an optimum value of C_S = 0.09, Moin and Kim [4] use C_S = 0.065 and Sullivan *et al*. [11] found $C_S \approx$ 0.12 to 0.13.

Discretization method is another issue to conduct LES in turbulence. A literature review suggests that the numerical method widely used for LES is the conventional finite difference method with structured grids [17-18]. For the time discretization of the Navier-Stokes equations explicit Runge-Kutta methods are a popular choice. Although they generally require the solution to a Poisson equation for the pressure at each stage, but Runge-Kutta methods have in general better stability properties, do not have a start-up problem, and easily allow for adaptive time stepping. The application of explicit Runge-Kutta methods to the incompressible Navier-Stokes equations is not straight forward because of the differential-algebraic nature of the equations. It is a common practice to explicitly advance the velocity at each stage as if the discretized equations are a system of ordinary differential equations, and subsequently solve a Poisson equation for the pressure to make the velocity field divergence-free [19].

A typical LES calculation for wall-bounded turbulent flows imposes a great demand on computation region, applying a low storage scheme is significant to make sufficient utilization of computer resource. Low-storage Runge-Kutta schemes require minimum levels of memory locations during the time integration and efficiently comply with the modern large-scale scientific computing needs. A number of explicit low-storage Runge-Kutta schemes of third-order accuracy were derived by Williamson [20].

Therefore, the objective of this study is to perform LES of a plane turbulent channel flow using Smagorinsky subgrid scale model and to discuss the effects of Smagorinsky constants. Spatial and temporal discretization has been done using the third order Low-Storage Runge-Kutta method and second order finite difference formulation respectively with staggered grid. We compare the

behavior of turbulence statistics with the DNS data of Moser et al. [2]. Then we discuss the contours of instantaneous streamwise velocity and streamwise shear velocity distribution of the flow at the centerline and immediate vicinity of the wall respectively for the three values of C_S. We also visualize the vortical structures using second invariant of the velocity gradient tensor in the turbulent flow field.

2. Governing Equations

The governing equations of LES for an incompressible plane channel flow are the filtered Navier-Stokes and continuity equations for constant density in Cartesian co-ordinates given as

$$\frac{\partial \overline{u}_i}{\partial t}+\frac{\partial}{\partial x_j}\left(\overline{u}_i.\overline{u}_j+\tau_{ij}\right)=-\frac{1}{\rho}\frac{\partial \overline{p}}{\partial x_i}+\frac{\partial}{\partial x_j}\left[\nu\left(\frac{\partial \overline{u}_i}{\partial x_j}+\frac{\partial \overline{u}_j}{\partial x_i}\right)\right], \text{ where } i, j = 1, 2, 3 \tag{1}$$

$$\frac{\partial \overline{u}_i}{\partial x_i}=0 \tag{2}$$

where the index i = 1, 2, 3 refers to the x, y and z directions respectively. Here $\overline{u}_x$, $\overline{u}_y$, $\overline{u}_z$ are streamwise, wall normal and spanwise filtered velocity respectively. $\overline{p}$ is the filtered pressure and ν is the kinematic viscosity. τ_{ij} is subgrid scale (SGS) Reynolds stress which is in fact the large scale momentum flux caused by the action of the small or unresolved scales. A schematic geometry of the plane turbulent channel flow and the co-ordinate system are shown in Fig. 1. The equations are non-dimensionalized by the channel half-width δ, and the wall shear velocity u_τ. The Reynolds number is therefore written as $Re = u_\tau.\delta/\nu$.

In LES, the velocity field u_i is decomposed into a large scale component $\overline{u}_i$ and a subgrid scale component u_i' by applying a spatial filtering operation. The resolved velocity component $\overline{u}_i$ can be expressed as follows:

$$\overline{u}_i(x_1,x_2,x_3,t)=\int_{-\infty}^{+\infty}\int_{-\infty}^{+\infty}\int_{-\infty}^{+\infty}\left(\prod_{i=1}^{3}G_i(x_i-x_i')\right)u_i(x_1',x_2',x_3',t)dx_1'\,dx_2'\,dx_3' \tag{3}$$

where $G_i(x_i-x_i')$ is a general filtering function which satisfies the following relation:

$$\int_{-\infty}^{+\infty}\int_{-\infty}^{+\infty}\int_{-\infty}^{+\infty}\left(\prod_{i=1}^{3}G_i(x_i-x_i')\right)dx_1'\,dx_2'\,dx_3'=1 \tag{4}$$

Since the continuity equation is linear, filtering does not change it significantly. However, it is important to note that $\overline{u_i.u_j}\neq\overline{u}_i.\overline{u}_j$, and the quantity on the left side of the inequality cannot be easily computed. So, a modeling approximation for the difference between the two sides of this inequality,

$$\tau_{ij}=\overline{u_i.u_j}-\overline{u}_i.\overline{u}_j \tag{5}$$

must be needed. The models used to approximate the SGS Reynolds stress are called subgrid scale (SGS) models. The most commonly used subgrid scale model is the Smagorinsky model. This model represents the SGS eddy viscosity according to

$$v_s = (C_S.\Delta)^2 |\bar{S}| . \tag{6}$$

Here C_S is the Smagorinsky constant, $\Delta = (\Delta x.\Delta y.\Delta z)^{1/3}$ is filter width and $|\bar{S}| = \sqrt{2\bar{S}_{ij}\bar{S}_{ij}}$ is the magnitude of strain rate, where $\bar{S}_{ij} = \frac{1}{2}\left(\frac{\partial \bar{u}_i}{\partial x_j} + \frac{\partial \bar{u}_j}{\partial x_i}\right)$. As we discussed in the introduction that the value of C_S is not fixed and the many authors used different values of C_S for LES in turbulent channel flows. Hence, to show the effects of the Smagorinsky constant for LES, in this study, the computation is performed and results are compared for three values of C_S such as 0.065, 0.1 and 0.13.

To reduce the near-wall eddy viscosity for the wall bounded flows the SGS eddy viscosity can be modified as:

$$v_s = (C_S.f_S.\Delta)^2 |\bar{S}| . \tag{7}$$

Here $f_S = 1 - \exp\left(-\frac{y^+}{A^+}\right)$ is the Van-Driest damping function, where y^+ is the distance from the wall in viscous wall units defined as $y^+ = \frac{y u_\tau}{v}$ and A^+ is a constant usually taken to be approximately 25 [15].

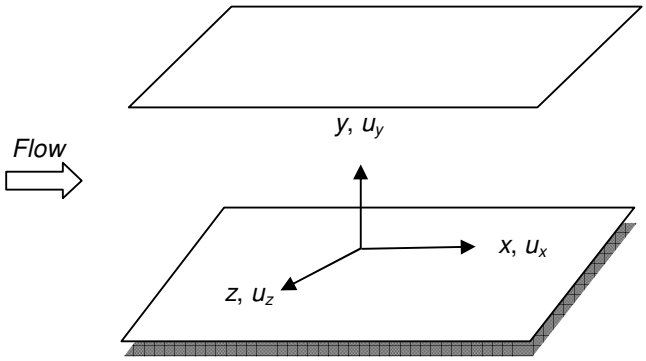

Fig. 1. Schematic geometry of plane channel flow

3. Numerical Method

The governing equations of LES are solved using the third order low-storage explicit Runge-Kutta method in time [21] and the second order finite difference formulae in space. The coupling between continuity equation and pressure fields is performed by the simplified marker-and-cell (SMAC) method [22]. Poisson equation is solved iteratively by a Preconditioned Incomplete Cholesky Decomposition Conjugated Gradient method. In the following subsections, staggered grid arrangement, discrete and interpolation operators are shortly introduced.

3.1 Staggered Grid Arrangement

Staggered grids may be constructed by several methods. An example of a staggered grid system in a two-dimensional plane is shown in Fig. 2. On the staggered grid, scalar variable pressure are stored at the nodes (intersection point of two lines) and velocities are defined at the middle of the two nodes. Horizontal (→) arrows indicate the locations for u_x – velocities and vertical (↑) ones denote those for u_y – velocities. The continuity is centered at pressure points. The momentum equation corresponding to each velocity component is centered at the respective velocity point [23]. The biggest advantage of the staggered arrangement is the strong coupling between the velocities and the pressure.

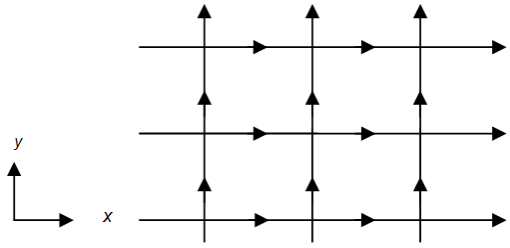

Fig. 2. Staggered grid system

In this study, the grid spacing in the periodic directions is uniform. The wall normal grid is stretched by using a hyperbolic-tangent type stretching function [23]:

$$Y(j)=\frac{tanh\left[\gamma\left(\frac{2j}{N}-1\right)\right]}{tanh(\gamma)},\ j=0,1,.....,N\ , \tag{8}$$

where the stretching parameter, γ is taken to be 2.25. Although here both uniform and stretched grids have been used but the order of accuracy is unaltered by mesh stretching.

3.2 Discrete Operators

There are a variety of discretization techniques available for developing discrete approximations to a set of governing partial differential equations such as Navier-Stokes equations. Let the finite difference operator of order one with stencil size 1 acting on a discrete variable φ with respect to x for structured Cartesian meshes with uniform spacing be defined as

$$\frac{\partial_1\varphi}{\partial_1 x}\Big|_{i,j,k}=\frac{\varphi_{i,j,k}-\varphi_{i-1,j,k}}{\Delta x} \tag{9}$$

where the grid spacings Δx are constant in x direction, and $(i,\ j,\ k)$ denotes associated mesh indices in x, y and z directions. Subscript "1" indices the stencil size. Discrete operators in the y and z – directions are similarly defined.

In addition to the discrete differencing operator we also define interpolation operators with stencil size 1 acting on a variable u_x in the x – direction as $\overline{u}_x^{1x}\Big|_{i,j,k}^{L}\equiv\frac{\overline{u}_x\big|_{i,j,k}+\overline{u}_x\big|_{i-1,j,k}}{2}$ and

$\overline{u}_x^{1x}\Big|_{i,j,k}^{R} \equiv \frac{\overline{u}_x\big|_{i,j,k} + \overline{u}_x\big|_{i+1,j,k}}{2}$, where L and R indicate the approximation of $\overline{u}_x^{1x}\Big|_{i,j,k}$ to the one-half left and right of the grid (i, j, k) in x – direction. The interpolation operator acting on the same variable $\overline{u}_x$ in y and z – directions are similarly defined. Interpolation operators acting on the other variables ($\overline{u}_y$ and $\overline{u}_z$) associated to the directions are defined similarly as above where (i, j, k) denotes associated mesh indices in x, y and z directions.

4 Computational Parameter and Grid Spacing

The computational domain of the mesh is selected to be $2\pi\delta \times 2\delta \times \pi\delta$ in streamwise, wall normal and spanwise directions respectively. The computation is carried out with $32 \times 64 \times 32$ grid points in the corresponding directions for a Reynolds number, Re_τ = 590 based on the channel half width, δ and wall shear velocity, u_τ. The computations are performed with non-dimensional time increment, Δt = 0.002, which maintained CFL numbers 0.791, 0.755 and 0. 911 for C_S = 0.065, 0.1 and 0.13 respectively. The CFL number is defined as $\mathrm{CFL} = \Delta t \max\left(\frac{|\langle\overline{u}_x\rangle|}{\Delta x} + \frac{|\langle\overline{u}_y\rangle|}{\Delta y} + \frac{|\langle\overline{u}_z\rangle|}{\Delta z}\right)$, where, $\langle\overline{u}_i\rangle$ denotes an ensemble average of $\overline{u}_i$. The computation is executed up to non-dimensional time, t = $n\,\Delta t$, where n is the number of time step. With the computational domain, the grid spacings in the streamwise and spanwise directions are $\Delta x^+ \approx 116$ and $\Delta z^+ \approx 58$ wall units respectively. In the wall normal direction $(-1 \le y \le +1)$ the minimum grid spacing is $\Delta y^+ \approx 2$ wall unit which exist at the immediate vicinity of the wall and maximum grid spacing is $\Delta y^+ \approx 42$ wall unit which exist at the centerline of the channel. The first mesh point away from the wall is at $y^+ \approx 0.885$ wall unit. The superscript '+' indicates a non-dimensional quantity scaled by the wall variables; e.g. $y^+ = y u_\tau / \nu$, where ν is the kinematic viscosity and $u_\tau = (\tau_w/\rho)^{1/2}$ is the wall shear velocity.

5 Boundary Conditions

We consider fully developed incompressible viscous flow and make use of periodic boundary conditions in the streamwise and spanwise directions. For the staggered grid arrangement we set up additional nodes surrounding the physical boundary. The calculations are performed at internal nodes only. The wall boundary condition is no-slip. Just outside the solution domain the values of the velocity components are equated to the values of the nearest node just inside the solution domain [24]. The pressure boundary condition is periodic in the streamwise and spanwise directions. But in the wall normal direction the values of $\overline{p}$, just outside the solution domain, are determined by assuming a zero gradient [25].

6 Temporal Schemes for LES in Plane Turbulent Channel Flow

Since the three components of the velocity vector $\boldsymbol{u}$ in the momentum equations are coupled with the pressure $\overline{p}$ through the continuity equation, these equations for the four variables $(\overline{u}_x, \overline{u}_y, \overline{u}_z, \overline{p})$ have to be solved at the same time. The temporal discretization used in our LES code for simulating the plane turbulent channel flow is the third order low storage explicit Runge-Kutta scheme [20] which is applied for the nonlinear convection and the viscous terms. This scheme

requires only two levels of memory locations during the time integration. Such a scheme reads the following sub-steps:

Sub-step 1:

$$\hat{u}_i^1 = \overline{u}_i^n + \alpha_1 \Delta t \overbrace{F_i\left(\overline{u}^n\right)}^{H_i^1} - \gamma_1 \frac{\Delta t}{\rho} \frac{\partial \overline{p}^n}{\partial x_i}$$

$$\frac{\partial \hat{u}_i^1}{\partial x_i} = 0$$

$$p^1 = \overline{p}^n - \psi^1$$

$$\overline{u}_i^1 = \hat{u}_i^1 + \gamma_1 \frac{\Delta t}{\rho} \frac{\partial \psi^1}{\partial x_i}$$

Sub-step 2:

$$\hat{u}_i^2 = \overline{u}_i^1 + \alpha_2 \Delta t \overbrace{F_i\left(\overline{u}^1\right)}^{H_i^2} + \beta_2 \Delta t H_i^1 - \gamma_2 \frac{\Delta t}{\rho} \frac{\partial p^1}{\partial x_i}$$

$$\frac{\partial \hat{u}_i^2}{\partial x_i} = 0$$

$$p^2 = p^1 - \psi^2$$

$$\overline{u}_i^2 = \hat{u}_i^2 + \gamma_2 \frac{\Delta t}{\rho} \frac{\partial \psi^2}{\partial x_i}$$

Sub-step 3:

$$\hat{u}_i^3 = \overline{u}_i^2 + \alpha_3 \Delta t F_i\left(\overline{u}^2\right) + \beta_3 \Delta t H_i^2 - \gamma_3 \frac{\Delta t}{\rho} \frac{\partial p^2}{\partial x_i}$$

$$\frac{\partial \hat{u}_i^3}{\partial x_i} = 0$$

$$p^3 = p^2 - \psi^3$$

$$\overline{u}_i^3 = \hat{u}_i^3 + \gamma_3 \frac{\Delta t}{\rho} \frac{\partial \psi^3}{\partial x_i}$$

where F_i $(i = x, y, z)$ are the convective and viscous terms and $\overline{u}_i$ $(i = x, y, z)$ are the velocity components. n is the level of time. The superscripts 1, 2, 3 on the variables represent the sub-step number. First equation of every sub-step is the momentum equation. Second equation is the Poisson equation for pressure. After the Poisson equation have been solved, pressure potential, ψ is found. The pressure potential is then used to calculate the pressure, $\overline{p}$ and velocity components from third and fourth equations respectively of every sub-step. Final solutions $\left(\overline{u}_x, \overline{u}_y, \overline{u}_z, \overline{p}\right)$ for every level of time are found from sub-step 3. Boundary conditions are assigned at every sub-step k. The Poisson equation for pressure at each sub-step can be written explicitly as follows:

$$\frac{\partial^2 p}{\partial x_j \partial x_j} = \frac{\rho}{\gamma_k \Delta t}\left[\overline{u}_i^{k-1} + \alpha_k \Delta t F_k\left(\overline{u}^{k-1}\right) + \beta_k \Delta t H_i^{k-1} - \hat{u}_i^k\right] \tag{10}$$

The values of α_k, β_k and γ_k are shown below:

$$\alpha_1 = \frac{8}{15} \qquad \beta_1 = 0 \qquad \gamma_1 = \frac{4}{15}$$
$$\alpha_2 = \frac{5}{12} \qquad \beta_2 = -\frac{17}{60} \qquad \gamma_2 = \frac{1}{15}$$
$$\alpha_3 = \frac{3}{4} \qquad \beta_3 = -\frac{5}{12} \qquad \gamma_3 = \frac{1}{6}$$

7 Results and Discussions

7.1 Turbulence Statistics

In this section we discuss some statistics of the computed flow field corresponding to the lower half of the 3D turbulent channel. The computed results in LES for all the three values of C_S are compared with the DNS data of Moser *et al*. [2]. Simulations are initialized with a random solenoidal velocity field and integrated ahead in time with finite viscosity.

Fig. 3 shows the mean velocity profiles of the LES and DNS data normalized by the wall-shear velocity which is defined as

$$u_x^+ = \frac{\langle \overline{u}_x \rangle}{u_\tau} \tag{11}$$

Numerous experiments have shown that the near-wall region can be largely subdivided into three layers. These three layers are the viscous sub-layer ($y^+ \leq 5$), buffer layer ($5 < y^+ \leq 30$) and logarithmic inertial layer ($y^+ > 30$) [15]. From Fig. 3 it can be observed that there is hardly noticeable difference between the DNS and LES results for all three cases in the viscous sub-layer. But here after in the buffer layer the LES results for all three values of C_S under predict the DNS result. Finally, in the logarithmic inertial layer the LES profiles are seen to be over predicted from DNS results. It is also revealed that in most of the regions the separation of LES velocity profiles from the DNS profile increases with the increase of the value of C_S. Nonetheless, Fig. 3 shows that the agreement of the mean velocity profile for C_S = 0.065 with the DNS data of Moser et al. [2] is good among these three values of C_S.

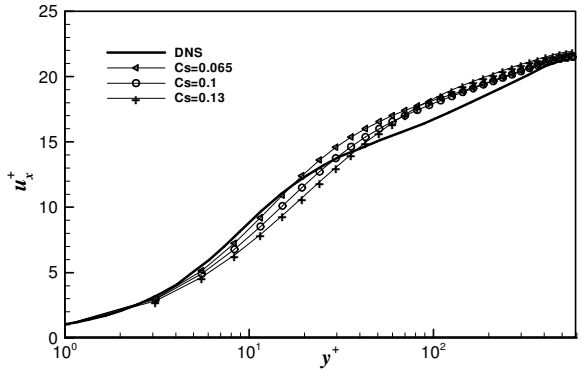

Fig. 3. The mean velocity profile in wall units normalized by the wall-shear velocity

The DNS and LES profiles of non-dimensional root mean square (*r.m.s.*) velocity components are displayed in Figs. 4(a, b, c), which are defined as

$$u^+_{x\,\text{r.m.s.}} = \sqrt{\left\langle \overline{u}_x^2 \right\rangle - \left\langle \overline{u}_x \right\rangle^2} \Big/ u_\tau \tag{12}$$

$$u^+_{y\,\text{r.m.s.}} = \sqrt{\left\langle \overline{u}_y^2 \right\rangle - \left\langle \overline{u}_y \right\rangle^2} \Big/ u_\tau \tag{13}$$

$$u^+_{z\,\text{r.m.s.}} = \sqrt{\left\langle \overline{u}_z^2 \right\rangle - \left\langle \overline{u}_z \right\rangle^2} \Big/ u_\tau \tag{14}$$

The streamwise root mean square velocity profiles are shown in Fig. 4(a) which reveals that there is hardly noticeable difference between the DNS and LES profiles in the viscous sub-layer. After that in rest of the domain the LES profiles over predict the DNS profile. Peak values of these profiles occur at the near wall region $\left(y^+ \approx 20-40\right)$. It has to be noted that in this region when the value of C_S increases, the peak value of the LES profiles decreases and the separation of the LES profiles from the DNS profile also decreases. After that in the region $\left(y^+ > 40\right)$, the LES profiles for C_S = 0.065 and 0.1 are almost collapsed and show closer agreement with the DNS results of Moser et al. [2]. The wall normal and spanwise root mean square velocity profiles are shown in Figs. 4(b) and 4(c). From these figures it can be observed that in the whole calculation domain the LES profiles under predict the DNS profile. It has to be noted that although there exists a noticeable discrepancy between the LES profiles at the near wall region, but away from the wall the computed profiles are almost collapsed with each other. However, the profiles of wall normal and spanwise root mean square velocity fields for C_S = 0.065 show less discrepancy from the DNS profile than that of the other two LES profiles.

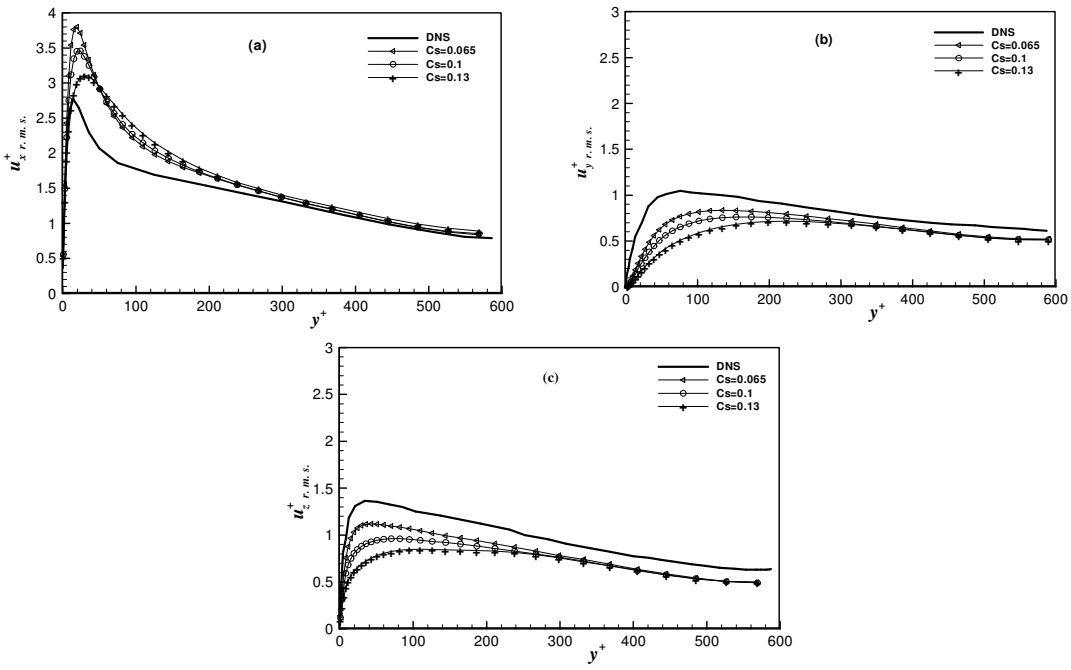

Fig. 4. Root mean square velocity profiles normalized by the wall-shear velocity

The profiles of non-dimensional Reynolds stress, $-\frac{\overline{u_x' u_y'}}{u_\tau^2}$ corresponding to the lower half of the channel are displayed in Fig. 5. This profile is a straight line in a fully developed channel flow when the flow reaches an equilibrium state. Our computed results clearly show that this is the case. Peak values of these profiles occur at the near wall region $(y^+ \approx 40-100)$ and the separation of the LES profiles from the DNS profile is higher in this region. It is noticeable that the separation from the DNS data increases with the increase of the value of C_S. This figure also reveals that when the value of C_S increases, the peak value of the Reynolds stress decreases and its position moves away from the wall. Away from the wall ($y^+ > 200$) there is hardly noticeable difference between the DNS and LES profiles. This figure clearly indicates that the Reynolds stress profile for C_S = 0.065 shows closer agreement with the DNS profile of Moser et al. [2].

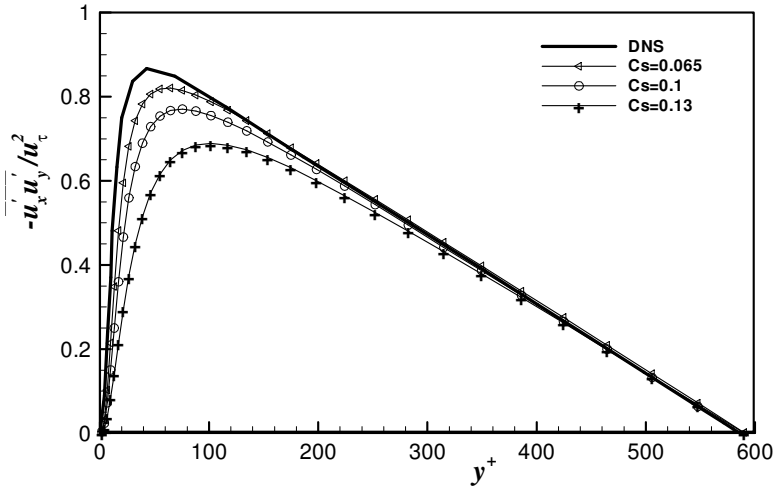

Fig. 5. The Reynolds stress profile in wall coordinates normalized by the wall-shear velocity

Table 1 provides a sample of the non-dimensional Reynolds stress at some positions in wall units which shows the quantitative comparison between the DNS and LES results. From this table it can be observed that the separation between the DNS and LES results increases with the increase of the value of C_S. It is also noticeable that away from the wall ($y^+ > 200$) the LES results show an excellent agreement with the DNS results. However, in the whole calculation domain the agreement of LES result with DNS for C_S = 0.065 is superior to that of the other two values of C_S.

Table 1. Comparison between DNS and LES results in Reynolds stress

y^+	DNS	LES		
		C_S = 0.065	C_S = 0.1	C_S = 0.13
4.30	0.09	0.07	0.05	0.03
26.66	0.80	0.68	0.56	0.37
42.95	0.87	0.80	0.72	0.57
101.78	0.80	0.79	0.76	0.69
224.21	0.60	0.60	0.59	0.56
386.24	0.34	0.34	0.33	0.32
547.65	0.07	0.07	0.06	0.07

7.2 Flow Structures

In this section we discuss about the computed streamwise velocity ($\overline{u}_x$) distribution at the centerline plane of the channel and streamwise shear velocity ($\overline{u}_{x\tau}$) distribution at the immediate vicinity of the wall at the end of calculation time for the three values of C_S. Using these computed data of LES, different contour plots of the flow field have been shown.

Contour of instantaneous streamwise velocity distributions at the centerline of the channel in x-z plane for C_S = 0.065, 0.1 and 0.13 respectively are shown in Figs. 6 (a, b, c). In these contour plots the value of $\overline{u}_x$ ranged between 19 and 24. The lowest value of $\overline{u}_x$ appears at blue regions, while the highest value of $\overline{u}_x$ appears at red regions in these contour plots. The higher values of $\overline{u}_x$ appear more densely adjacent to the centerline of the channel from both sides. It can be observed that the intensity of streamwise velocity increases with the increase of the value of C_S.

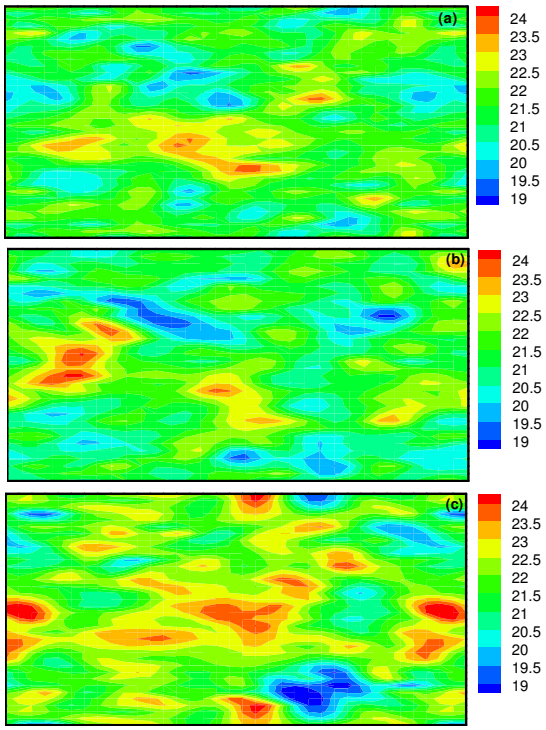

Fig. 6. Contours of streamwise velocity profiles in x-z plane for (a) C_S = 0.065, (b) C_S = 0.1 and (c) C_S = 0.13.

Streamwise Shear Velocity ($\overline{u}_{x\tau}$) distribution at the immediate vicinity of the wall of this channel can be calculated using (15).

$$\overline{u}_{x\tau} = \sqrt{\frac{\tau_x}{\rho}} \tag{15}$$

where, $\overline{u}_{x\tau}$ = streamwise shear velocity
ρ = density of the fluid
τ_x = streamwise shear stress.

Contour of the instantaneous streamwise shear velocity ($\overline{u}_{x\tau}$) distribution in x-z plane for C_S = 0.065, 0.1 and 0.13 respectively are displayed in Figs. 7 (a, b, c). In these contour plots the value of $\overline{u}_{x\tau}$ ranged between 0.7 and 2.0. The highest value of $\overline{u}_{x\tau}$ is indicated by a red color, while the lowest value of $\overline{u}_{x\tau}$ is indicated by a blue color in these contour plots. The lower values of streamwise shear velocity appear more densely away from the centerline of this channel. It is also noticeable that the intensity of streamwise shear velocity increases with the increase of the value of C_S.

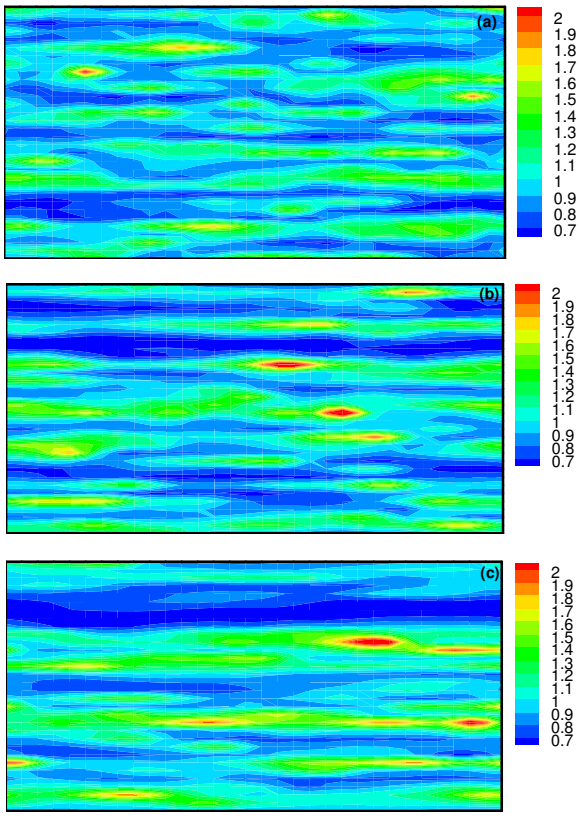

Fig. 7. Contours of streamwise shear velocity profiles in x-z plane for (a) C_S = 0.065, (b) C_S = 0.1 and (c) C_S = 0.13

Figs. 8 (a, b, c) represent the visualization of vortical structures in the turbulent channel flow by iso-surfaces of the second invariant Q of velocity gradient tensor for C_S = 0.065, 0.1 and 0.13 respectively. The second invariant Q is defined as:

$$Q = -\frac{1}{2}\left(S_{ij}.S_{ij} - \Omega_{ij}.\Omega_{ij}\right) \tag{16}$$

where, $S_{ij} = \frac{1}{2}\left(\frac{\partial \overline{u}_i}{\partial x_j} + \frac{\partial \overline{u}_j}{\partial x_i}\right), \Omega_{ij} = \frac{1}{2}\left(\frac{\partial \overline{u}_i}{\partial x_j} - \frac{\partial \overline{u}_j}{\partial x_i}\right)$ (17)

are the strain-rate and rotation tensors respectively, which are the symmetric and asymmetric part of the velocity gradient tensor:

$$A_{ij} = \frac{\partial u_i}{\partial x_j} = S_{ij} + \Omega_{ij} \tag{18}$$

The visualized region is the whole calculation domain. For all three values of C_S the level of the iso-surface is chosen to be Q = 5. For this value of Q the flow field contains lots of tube-like vortical structures which are randomly distributed over the turbulent flow field. Generally, it can be noted that for all values of C_S the vortices are generated more intensely in between near the boundary and the centerline of the channel than that in the position of around the centerline of the channel. It is also noticeable that the vortices are generated more intensely for C_S = 0.1 than that of the other two values of C_S.

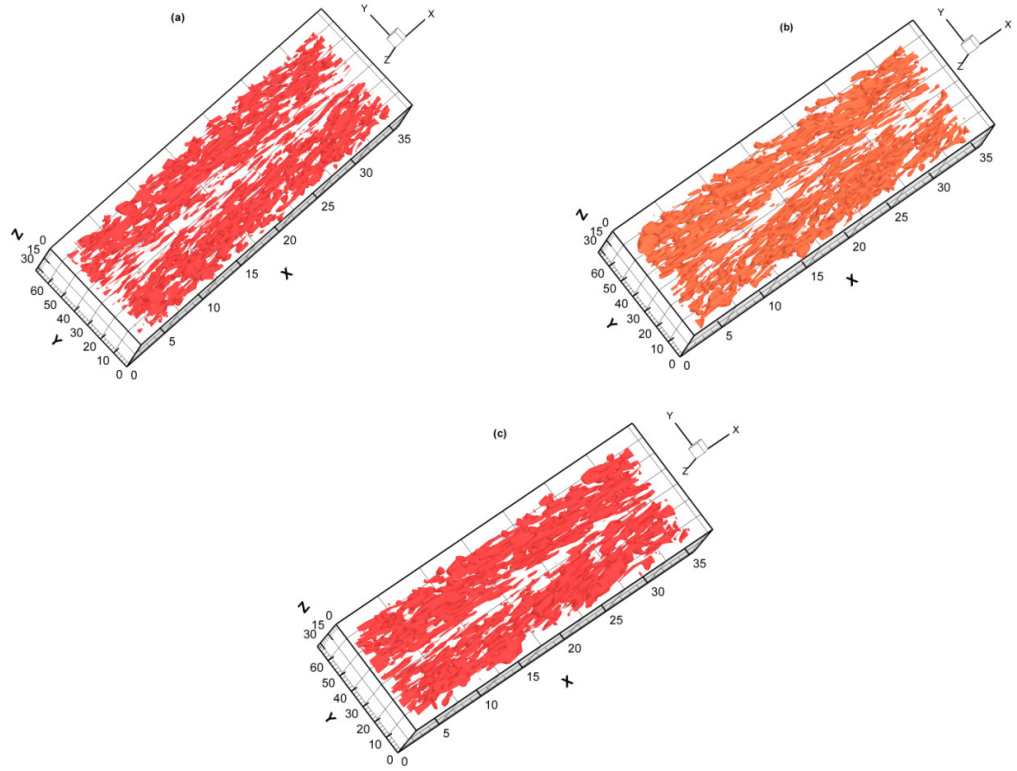

Fig. 8. Iso-surfaces of the second invariant (Q =5) in the channel flow for (a) C_S = 0.065, (b) C_S = 0.1 and (c) C_S = 0.13

8 Conclusions

A Large eddy simulation of a turbulent channel flow has been successfully performed using the Smagorinsky subgrid scale model for three different values of Smagorinsky constant at a Reynolds number, Re_τ = 590 with $32 \times 64 \times 32$ grid points. Essential turbulence statistics have been calculated and compared the results with the DNS data of reference, which show reasonable agreement with the DNS results. After analyzing the results of turbulence statistics throughout the whole calculation domain we have found that among the three values of C_S = 0.065, 0.1 and 0.13, the performance of Smagorinsky model for C_S = 0.065 is superior to that of the other two Smagorinsky

constants. However, away from the wall the computed results for all three cases show a good agreement with the DNS results. Instantaneous streamwise velocity distribution at the centerline plane of the channel and streamwise shear velocity distribution at the immediate vicinity of the channel have also been measured in the contour plots for all values of C_S. Higher values of streamwise velocity appear more densely adjacent to the centerline of the channel from both sides and lower values of streamwise shear velocity appear more densely away from the centerline of this channel. The intensities of streamwise velocity and streamwise shear velocity distributions increase with the increase of the value of C_S. Visualization of the iso-surfaces of the second invariant Q in the turbulent channel flow show that the flow field contains lots of tube-like vortical structures which are significant and randomly distributed over the turbulent flow field. For all three values of C_S the intensity of the vortical structures in the turbulent flow field is high in between near the boundary and the centerline of the channel.

Competing Interests

Authors have declared that no competing interests exist.

References

[1] Kim J, Moin P, Moser R. Turbulence statistics in fully developed channel flow at low Reynolds number. Journal of Fluid Mechanics. 1987;177:133-166.
DOI: dx.doi.org/10.1017/S0022112087000892.

[2] Moser RD, Kim J, Mansour NN. Direct numrical simulation of turbulent channel flow up to Re_τ = 590. Physics of Fluids.1999;11(4):943-945. DOI: 10.1063/1.869966.

[3] Deardorff JW. A Numerical study of three-dimensional turbulent channel flow at large Reynolds numbers. Journal of Fluid Mechanics. 1970;41:453-465.

[4] Moin P, Kim J. Numerical Investigation of Turbulent Channel Flow. Journal of Fluid Mechanics. 1982;118:341-377.
Available: http://dx.doi.org/10.1017/S0022112082001116

[5] Mallik MSI, Uddin MA, Meah MA. Large eddy simulation of turbulent channel flow at Re_τ = 590. IOSR Journal of Mathematics. 2014;10(6):41-50. DOI:10.9790/5728-10644150.

[6] Yang F, Zhang HQ, Chan CK, Wang XL. Large eddy simulation of turbulent channel flow with 3d roughness using a roughness element model. Chinese Physics Letters. 2008;25 (1):191-194.
Available: http://dx.*doi*.org/10.1088/0256-307X/*25*/*1*/052

[7] Piomelli U, Moin P, Ferziger JE. Model consistency in large eddy simulation of turbulent channel flows. Physics of Fluids. 1988;31:1884-1891.

[8] Piomelli U, Balaras E. Wall-layer models for large-eddy simulations. Annual Review of Fluid Mechanics. 2002;34:349-374. DOI: 10.1146/annurev.fluid.34.082901.144919.

[9] Xie Z, Lin B, Falconer RA. Large-eddy simulation of the turbulent structure in compound open-channel flows. Advances in Water Resources. 2013;53:66-75.
DOI: org/10.1016/j.advwatres.2012.10.009.

[10] Gungor AG. A new two-scale model for large eddy simulation of wall-bounded flows. Doctoral Diss. Georgia Institute of Technology; 2009.

[11] Sullivan PP, McWilliams JC, Moeng C. A subgrid-scale model for large-eddy simulation of planetary boundary-layer flows. Boundary-Layer Meteorology. 1994;71:247-276. DOI: 10.1007/BF00713741.

[12] Horiuti K. A proper velocity scale for modeling subgrid-scale eddy viscosities in large eddy simulation. Physics of Fluids. 1993;5:146-157. DOI: 10.1063/1.858800.

[13] Yakhot A, Orszag S, Yakhot V, Israeli M. Renormalization group formulation of large-eddy simulations. Journal of Scientific Computing. 1989;4:139-158.

[14] Bardina J, Ferziger JH, Reynolds WC. Improved turbulence models based on large eddy simulation of homogeneous, incompressible, turbulent flows. Report TF-19, Thermosciences Division, Stanford University; 1983.

[15] Sagaut P. Large eddy simulation for incompressible flows: An Introduction. Berlin Heidelberg: Springer-Verlag; 2001.

[16] Scotti A, Meneveau C, Lilly DK. Generalized smagorinsky model for anisotropic grids. Physics of Fluids. 1993;5:2306-2308.

[17] Ham FE, Lien FS, Strong AB. A fully conservative second-order finite difference scheme for incompressible flow on nonuniform grids. Journal of Computational Physics. 2002;177:117-133. DOI: 10.1006/jcph.2002.7006.

[18] Morinishi Y. Skew-symmetric form of convective terms and fully conservative finite difference schemes for variable density low-Mach number flows. Journal of Computational Physics. 2010;229:276-300. DOI>10.1016/j.jcp.2009.09.021.

[19] Sanderse B, Koren B. Accuracy analysis of explicit Runge-Kutta methods applied to the incompressible Navier-Stokes equations. Journal of Computational Physics. 2012;231:3041-3063.
Available: http://dx.*doi*.org/10.1016/j.jcp.2011.11.028

[20] Williamson JH. Low-storage Runge-Kutta schemes. Journal of Computational Physics. 1980;35:48-56. DOI: 10.1016/0021-9991(80)90033-9.

[21] Kennedy CA, Carpenter MH, Lewis RM. Low-storage, explicit Runge-Kutta schemes for the compressible Navier-Stokes equations. Applied Numerical Mathematics. 2000;35:177-219. DOI>10.1016/S0168-9274(99)00141-5.

[22] Johnson DB, Raad PE, Chen S. Simulation of impacts of fluid free surfaces with solid boundaries. International Journal for Numerical Methods in Fluids. 1994;19:153-176. DOI: 10.1002/fld.1650190205.

[23] Morinishi Y, Lund TS, Vasilyev OV, Moin P. Fully conservative higher order finite difference schemes for incompressible flow. Journal of Computational Physics. 1998;143:90-124. DOI>10.1006/jcph.1998.5962.

[24] Versteeg HK, Malalasekera W. An introduction to computational fluid dynamics. England: Longman Group Limited; 1995.

[25] Anderson Jr JD. Computational fluid dynamics. New York: McGraw-Hill; 1995.

Peer-review history:
The peer review history for this paper can be accessed here (Please copy paste the total link in your browser address bar)
www.sciencedomain.org/review-history.php?iid=936&id=6&aid=8300